航測及遙測學刊　第三十一卷　第 1 期　第 1-19 頁　民國 115 年 3 月
Journal of Photogrammetry and Remote Sensing
Volume 31, No.1, 2026, pp. 1-19
DOI：10.6574/JPRS.202603_31(1).0001

Integrated Optical–SAR Texture Analysis for Neural Network–Based Emergency Landslide Surveying and Mapping

Yi-Keng Chen [1*]　　Shou-Hao Chiang [2]

Abstract

Optical remote sensing imagery provides critical spectral information for mapping landslide inventories but is frequently hindered by cloud cover and adverse weather. In contrast, Synthetic Aperture Radar (SAR) penetrates clouds and is highly sensitive to surface backscatter changes, offering complementary insights for detecting landslide disturbances. This study presents an integrated approach combining optical and SAR data to enable rapid and reliable landslide detection under challenging conditions. The proposed framework applies object-based image analysis (OBIA) to segment terrain into meaningful units and derives $NDVI_{diff}$ and NDSI indices from pre- and post-event imagery, together with six GLCM-based texture features, to characterize surface disturbances. Four classification scenarios, including optical-only, SAR-only, cloud-obstructed optical, and fusion-based models, were systematically compared. Results demonstrate that the fusion approach consistently yields more spatially coherent and complete landslide inventories, while SAR-based mapping alone successfully delineates most large-scale landslides under heavy cloud cover. These findings confirm the operational effectiveness of the proposed optical–SAR framework for rapid, event-driven landslide mapping and disaster risk assessment.

Keywords: Landslide Detection, Synthetic Aperture Radar, Image Texture, Image Fusion, Artificial Neural Network

1. Introduction

Satellite-based emergency mapping (SEM) has become a cornerstone of disaster risk reduction, enabling governments and researchers to rapidly assess hazard impacts and plan relief operations. Over recent decades, SEM has evolved into an integral component of broader resilience strategies aimed at improving the timeliness and effectiveness of emergency response and minimizing human and economic losses during and after catastrophic events.

Taiwan, located in the subtropical monsoon region, is highly susceptible to typhoon-induced landslides and debris-flow disasters. From July to September, intense rainfall frequently triggers large-scale slope landslides in its mountainous areas, dramatically transforming land cover from vegetated slopes to bare soil. Optical satellite imagery has long been used to detect such changes because of its rich spectral content and the strong radiometric contrast between vegetation and landslides under clear daylight conditions. High-resolution satellite-based sensors such as LANDSAT, SPOT, and FORMOSAT, often combined with digital elevation models (DEMs), have further enabled three-dimensional visualization and both manual and automated mapping of landslides. However, persistent cloud cover, typhoons, and thunderstorms during Taiwan's summer can delay the availability of optical data precisely when emergency landslide mapping is most needed.

Synthetic Aperture Radar (SAR), operating in the microwave domain, mitigates this limitation by penetrating cloud cover and acquiring data both day and night. SAR thus provides complementary information on surface roughness and backscatter changes that is valuable for landslide and debris-flow detection under adverse weather. Yet, SAR imagery also poses interpretive challenges due to speckle noise, geometric distortions, and sensitivity to polarization and observation geometry. In emergency landslide mapping, optical imagery is often hindered by cloud cover and adverse weather conditions. However, cloud contamination is typically spatially heterogeneous and temporally variable, and partially cloud-free or multi-temporal optical observations can still provide useful complementary information. By integrating such heterogeneous inputs with weather-independent SAR data, fusion supports rapid initial assessment and subsequent refined delineation. When optical data are severely limited, SAR-derived features dominate the fusion process, whereas under favorable conditions, optical imagery enhances spatial accuracy.

[1] Ph.D. Student, Department of Civil Engineering, National Taiwan University
[2] Associate Professor, Center for Space and Remote Sensing Research, National Central University
[*] Corresponding Author, E-mail: d10521008@ntu.edu.tw

Received Date: Oct. 15, 2025
Revised Date: Jan. 07, 2026
Accepted Date: Feb. 04, 2026

These contrasting advantages and limitations of optical and SAR imagery motivate the development of fusion approaches specifically designed for time-critical, event-based landslide mapping rather than routine monitoring. Image fusion integrates multi-source remote sensing data to improve measurement accuracy, enhance information content, and increase interpretive reliability. In terms of data quality, optical imagery generally provides higher radiometric contrast and spectral sensitivity for landslide detection under clear-sky conditions, enabling accurate delineation of disturbed surfaces. However, its performance is frequently degraded by cloud cover, terrain shadow, and illumination variability during typhoon and monsoon seasons. In contrast, SAR imagery offers stable, weather-independent observations and ensures reliable data availability under adverse conditions, although it is affected by speckle noise and geometric distortions in mountainous terrain. These complementary characteristics justify the combined use of optical and SAR data for robust emergency landslide mapping. This study advances emergency landslide mapping by introducing an Artificial Neural Network (ANN)–based image fusion framework implemented within an object-based image analysis (OBIA) environment. ANN approaches are particularly suited to this task because they can model complex, non-linear relationships and spatial heterogeneities more effectively than traditional classifiers. By leveraging ANN's capacity to learn from diverse input features, the proposed framework fuses the complementary strengths of optical and SAR datasets at the decision level, thereby avoiding the co-registration difficulties common in rugged terrain.

The objectives of this study are threefold: (1) to fuse optical and SAR remote sensing information to improve the accuracy and reliability of event-based emergency landslide and debris-flow detection; (2) to assess the applicability of incorporating SAR data into classification models when optical images are limited during crises; and (3) to provide a replicable workflow for rapid, event-driven landslide mapping that can be adapted to other disaster types and geographic settings. By focusing on the operational requirements of emergency mapping, this research contributes a novel, robust, and scalable methodology to advance satellite-based disaster response.

2. Literature Reviews

Landslide inventory mapping is a cornerstone of hazard assessment in Taiwan, where slopes fail under heavy rainfall, earthquakes, and anthropogenic pressures such as deforestation and intensive land use (Selby, 1993; Dai & Lee, 2002). Optical satellites, often combined with DEM, have long enabled visual delineation of landslides by exploiting spectral contrasts between vegetation and bare soil (Haeberlin *et al.*, 2004; Nichol *et al.*, 2006). The normalized difference vegetation index, NDVI and its temporal differential $NDVI_{diff}$ (Chen, 2019) have proven effective in detecting fresh landslides by highlighting vegetation loss (Weier & Herring, 2000). Yet, optical systems falter under cloud cover, shadows, or low illumination—conditions common during typhoon events.

SAR offers compelling advantages for disaster mapping: all-weather, day–night imaging with sensitivity to surface roughness and backscatter changes. Conventional differential interferometry synthetic aperture radar, Differential Interferometry Synthetic Aperture Radar (DInSAR) has been effective for creeping landslides but is less reliable for abrupt, collapse-type landslides induced by heavy rainfall (Colesanti & Wasowski, 2006). Backscatter-based approaches, including Polarimetric Synthetic Aperture Radar (PolSAR) and the Sigma-naught coefficient, yield richer scattering information and, when differenced as NDSI, can delineate sharp land surface changes (Furuta & Tomiyama, 2008; Guzzetti *et al.*, 2012). However, SAR data are affected by speckle noise, geometric distortions, and sensitivity to acquisition parameters. Recent studies have further investigated the applicability of multi-sensor and multi-geometry SAR observations in complex terrain, demonstrating their potential for landslide detection under diverse acquisition conditions (Wang *et al.*, 2025).

Image fusion offers a path forward by integrating complementary strengths of optical and SAR data to enhance classification robustness (Pohl & van Genderen, 1998; Amarsaikhan & Douglas, 2004). However, pixel- and feature-level fusion demand high co-registration accuracy—untenable in complex mountainous terrains. Decision-level fusion, which integrates classification results rather than raw pixels, is more tolerant of misalignment but remains underutilized for landslide mapping. Recent advances echo these challenges. Jin *et al.* (2022) fused multisource data (DEM, spectral and backscatter features) to improve landslide classification accuracy. Zhang & Wang (2024) reviewed deep learning-based landslide detection, emphasizing difficulties in generalization and domain shift between sensors. Li & Xiao (2025) surveyed fusion of optical, SAR, and LiDAR for landslide mapping, highlighting the potential of hybrid networks but noting challenges in aligning modalities. Prakash *et al.* (2020) systematically compared deep learning and traditional machine learning approaches for landslide mapping using Earth observation data, demonstrating the advantages of deep architectures in complex environments. Chen *et al.* (2023) proposed a multi-input channel U-Net framework integrating

multisource SAR data, achieving improved detection performance through feature-level fusion. Liu *et al.* (2024) developed an attention-based Swin Transformer U-Net for landslide segmentation, highlighting the effectiveness of transformer architectures in capturing multi-scale contextual information. Tuo *et al.* (2025) further explored multimodal data fusion using an improved DeepLabv3+ model, demonstrating enhanced segmentation accuracy through integrated optical and SAR features. In addition, Fu *et al.* (2024) combined Sentinel-1 SAR and Sentinel-2 optical imagery for landslide dating, illustrating the value of multi-temporal and multi-sensor integration in post-event analysis. Coluzzi *et al.* (2025) proposed a robust change detection technique based on freely available optical imagery for rapid landslide identification, while Jiang *et al.* (2025) provided a comprehensive review of deep learning–based landslide detection, summarizing recent progress, challenges, and future opportunities.

These works indicate that while multisensor fusion and deep learning methods are advancing, most existing approaches rely on complex network structures, extensive training data, and precise preprocessing, which limit their applicability in time-critical emergency scenarios. Consequently, operational, cloud-robust frameworks that combine optical and SAR for emergency landslide mapping remain scarce. Building on this body of work, the present study introduces an ANN-driven, decision-level fusion within an OBIA framework, integrating $NDVI_{diff}$ and NDSI with texture features to (i) bypass strict co-registration demands, (ii) exploit complementary spectral and backscatter cues under cloudy conditions, and (iii) support rapid, reliable event-based landslide detection in steep, cloud-prone landscapes.

3. Methodology

In response to the need for rapid, event-driven landslide assessment, this study implements an ANN-based, decision-level image fusion within an OBIA framework to support emergency landslide mapping in the Laonong River watershed, southern Taiwan, which experienced extensive slope landslides and debris flows during Typhoon Morakot in 2009. The workflow comprises the following steps: (1) image segmentation to generate object units and texture features; (2) selection of representative training samples; and (3) supervised classification using a back-propagation multilayer perceptron. This integrated procedure operationalizes the proposed framework for rapid and reliable landslide detection during emergency conditions.

3.1 Research Materials

3.1.1Pixel-based Evaluation

FORMOSAT-2, Taiwan's first Earth observation satellite, provided high-resolution (2 m PAN, 8 m MS) multispectral imagery suitable for landslide monitoring. For this study, three geometrically corrected images were acquired to represent Typhoon Morakot conditions: a pre-event scene (9 May 2009), a post-event scene with minimal cloud (12 Sept 2009), and a cloud-obstructed scene captured soon after the typhoon (15 Aug 2009) to simulate emergency mapping scenarios (Figure 1). Because the 15 Aug 2009 image exhibited extensive cloud cover, the pre-processing of the $NDVI_{diff}$ image modified the cloud-covered areas by masking and assigning them a value of "0" to prevent misclassification during analysis. Leveraging these datasets, temporal changes in vegetation cover were quantified using the $NDVI_{diff}$ index, which highlights vegetation loss and newly exposed soil attributable to the typhoon. By differencing pre- and post-event NDVI values, $NDVI_{diff}$ provides a robust measure of surface change despite seasonal or illumination variations, thereby supporting event-driven landslide detection. The formulas of NDVI and $NDVI_{diff}$ are as follows:

$$\mathrm{NDVI} = \frac{\mathrm{NIR}-\mathrm{Red}}{\mathrm{NIR}+\mathrm{Red}} \quad \text{..... (1)}$$

$$\mathrm{NDVI_{diff}} = \mathrm{NDVI_{post}} - \mathrm{NDVI_{pre}} \quad \text{..... (2)}$$

Where NIR and Red denote the spectral reflectance in the near-infrared and red bands, respectively. $NDVI_{post}$ and $NDVI_{pre}$ represent post- and pre-event NDVI values. $NDVI_{diff}$ (Figure 2) highlights temporal changes in vegetation cover, enabling the detection of newly exposed soil or disturbed areas such as landslides.

3.1.2SAR Image

ALOS/PALSAR L-band SAR data from 8 Jul. 2009 (pre-event) and 23 Aug. 2009 (post-event) (Figure 3) were selected because their longer wavelength penetrates vegetation more effectively than C-band sensors, providing clearer information on ground conditions in heavily forested terrain. Radar backscatter intensity reflects surface roughness, moisture, and slope orientation, producing higher returns from areas directly facing the sensor and lower returns from opposing slopes. To extract meaningful ground signals, raw SAR images underwent radiometric calibration, geometric correction with a DEM, and speckle filtering to reduce noise. The normalized difference sigma-naught index (NDSI) was then computed from pre- and post-event backscatter coefficients to quantify changes in scattering properties, as expressed by:

$$NDSI = \frac{\sigma_m^0 - \sigma_s^0}{\sigma_m^0 + \sigma_s^0} \quad \text{..... (3)}$$

where $\sigma_m{}^0$ denotes the master sigma-naught (Sigma0) image representing the post-typhoon event and $\sigma_s{}^0$ denotes the slave sigma-naught image representing the pre-typhoon event. Extreme positive or negative NDSI values (Figure 4) highlight abrupt surface disturbances—such as fresh landslides—whereas stable terrain remains near zero, making NDSI a robust indicator of event-driven ground change and a valuable complement for rapid landslide detection. Because the primary focus of this study is slope landslides rather than sediment deposition within river channels, all NDSI values in river areas were assigned zero.

The original ALOS/PALSAR Level 1.1 imagery used in this study was acquired in Fine mode with a spatial resolution of approximately 14 m. To ensure spatial consistency with the digital elevation model (DEM) and optical datasets, geometric correction and terrain normalization were performed using a 10 m DEM. During this process, the original SAR images were resampled from 14 m to 10 m using bilinear interpolation. Consequently, all subsequent analyses were conducted on harmonized 10 m resolution data, thereby minimizing scale discrepancies among multi-source datasets and facilitating consistent object-based segmentation and feature extraction within the proposed fusion framework.

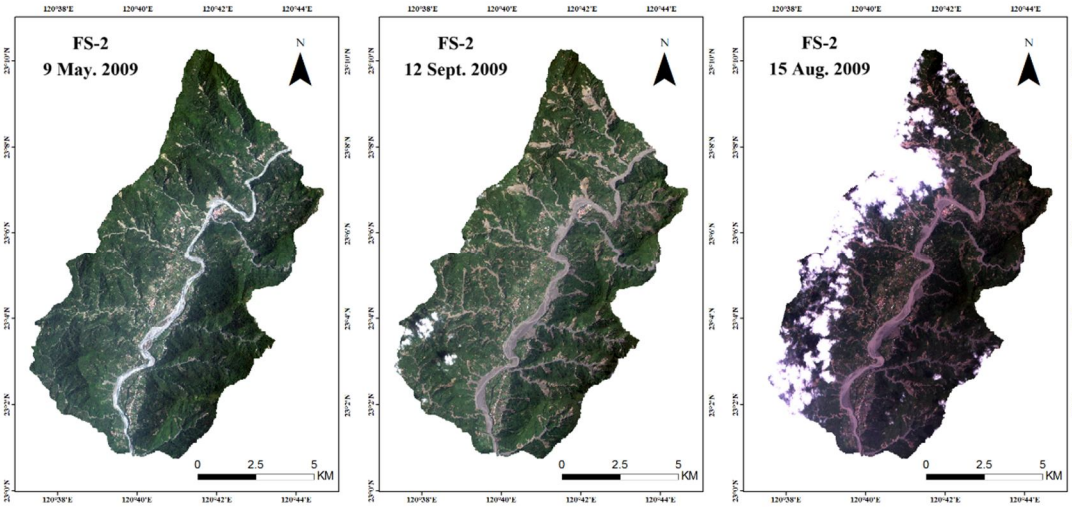

Figure 1 FORMOSAT-2 imagery. Left: 9 May 2009 (pre–Typhoon Morakot); Center: 12 Sept. 2009 (post-event); Right: 15 Aug. 2009 (post-event). The cloud cover and missing southwestern area in the right image provide conditions suitable for simulating emergency mapping

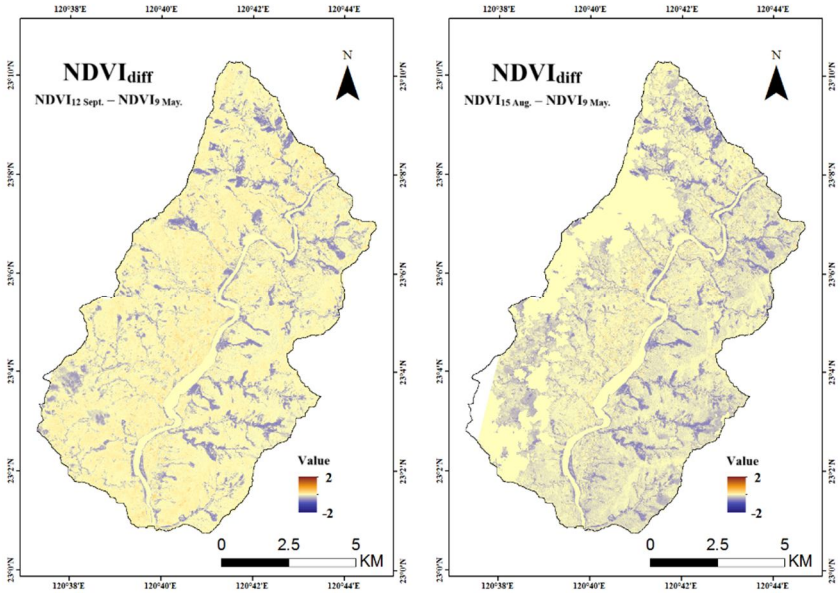

Figure 2 $NDVI_{diff}$ imagery. Left: $NDVI_{diff}$-0912 image, generated by "$NDVI_{12\ Sept.} - NDVI_{9\ May.}$"; Right: $NDVI_{diff}$-0815 image, generated as "$NDVI_{15\ Aug.} - NDVI_{9\ May.}$," with cloud-covered areas masked and assigned a value of "0" to prevent misclassification

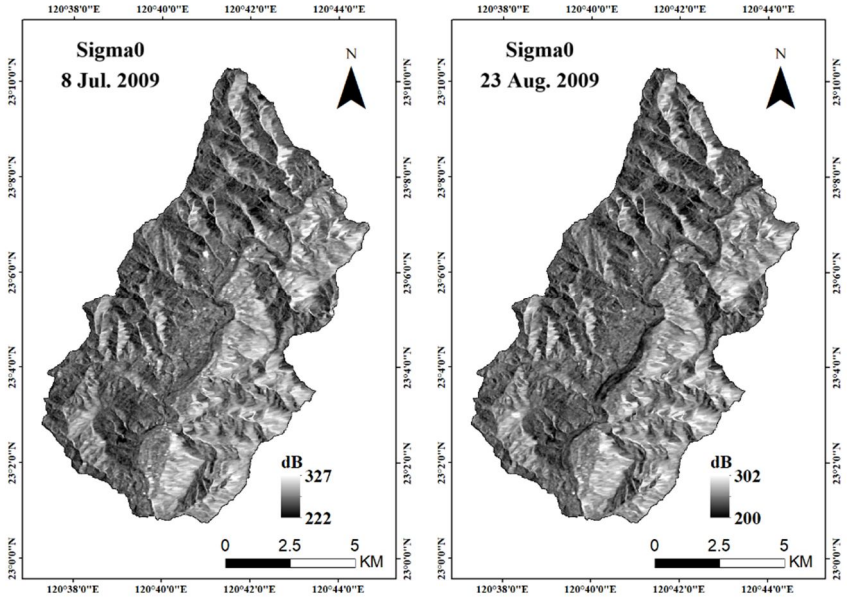

Figure 3 ALOS/PALSAR Sigma0 imagery. Left: σ^0_{0708} image; Right: σ^0_{0823} image

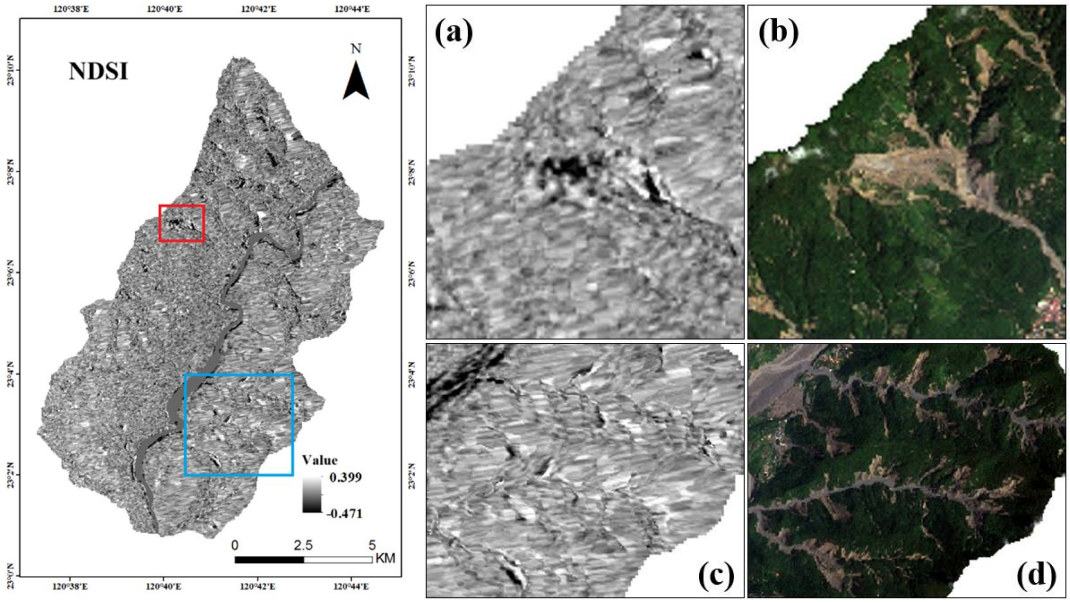

Figure 4 NDSI image. The red and blue boxes indicate areas enlarged for detailed comparison: (a) NDSI texture of landslides within the red box; (b) corresponding reference photograph of the red-box landslides; (c) NDSI texture of landslides within the blue box; and (d) corresponding reference photograph of the blue-box landslides

3.1.3Landslide Inventory

The original 1:5000-scale landslide inventory map compiled from post-Morakot stereoscopic aerial photographs (SWCB, 2011) included many pre-existing landslides and thus did not accurately represent event-induced landslides. In this study, the landslide inventory (Figure 5) was revised by extracting areas of significant $NDVI_{diff}$ decrease and cross-referencing them with the original map, FORMOSAT-2 imagery, and high-resolution Google Earth images to manually delineate and retain only landslides triggered by Typhoon Morakot.

3.2 Image Segmentation

Multiresolution segmentation is applied as the initial step in object-based landslide delineation. This bottom-up region-growing algorithm aggregates adjacent pixels based on scale, shape, and compactness, allowing adaptive object sizes suited to the complex geometry of mass movements (Ez-zahouani *et al.*, 2023; Tetteh *et al.*, 2023). For large scale landslides, each landslide is segmented into roughly three to five clusters, capturing internal variability without excessive fragmentation (Table 1). Object-level textures are then derived from the Gray Level Co-

occurrence Matrix (GLCM) (Haralick *et al.*, 1973), producing descriptors such as contrast, dissimilarity, entropy, and homogeneity that, combined with spectral indices, enhance representation of surface roughness and structural complexity. This integration provides robust inputs for ANN-based optical–SAR fusion and rapid emergency landslide mapping.

To enhance the discriminatory power of the segmented objects, six GLCM-derived texture features were selected to capture tonal variation, surface roughness, and internal complexity—key traits distinguishing landslide deposits from stable terrain (Table 2). These descriptors complement spectral indices by quantifying abrupt and gradual spatial changes within each segment, enhancing classification reliability. The description and formulas of texture features are as follows:

(1) **Contrast:** highlights abrupt tonal changes, accentuating fresh landslide and rough debris surfaces.

(2) **Dissimilarity:** linearly measures gray-level variation, capturing gradual differences within landslide bodies.

(3) **Entropy:** reflects randomness and complexity, indicating heterogeneous disturbed slopes versus stable terrain.

(4) **Homogeneity:** measures smoothness, distinguishing intact areas from disrupted ground.

(5) **Mean:** represents average brightness, revealing differences between exposed soil and vegetated patches.

(6) **Standard Deviation:** quantifies value dispersion, identifying mixed materials typical of mass-movement deposits.

$$\mathbf{P}_{i,j} = \frac{V_{i,j}}{\sum_{i,j=0}^{N-1} V_{i,j}} \quad \text{..... (4)}$$

$$\text{Contrast} = \sum_{i,j=0}^{N-1} \mathbf{P}_{i,j}(i-j)^2 \quad \text{..... (5)}$$

$$\text{Dissimilarity} = \sum_{i,j=0}^{N-1} \mathbf{P}_{i,j}|i-j| \quad \text{..... (6)}$$

$$\text{Entropy} = \sum_{i,j=0}^{N-1} \mathbf{P}_{i,j}(-\ln \mathbf{P}_{i,j}) \quad \text{..... (7)}$$

$$\text{Homogeneity} = \sum_{i,j=0}^{N-1} \frac{\mathbf{P}_{i,j}}{1+(i-j)^2} \quad \text{..... (8)}$$

$$\text{Mean } \mu = \frac{1}{N}\sum_{i,j=1}^{N} V_{i,j} \quad \text{..... (9)}$$

$$\text{Standard Deviation} = \sqrt{\frac{1}{N}\sum_{i,j=1}^{N}(V_{i,j}-\mu)^2} \quad \text{..... (10)}$$

Where, ***P*** denotes the gray level co-occurrence matrix; *i* and *j* represent the row and column indices, respectively; $V_{i,j}$ is the pixel value at cell i, j within the image segment; $\boldsymbol{P_{i,j}}$ is the normalized value at cell i, j; and *N* is the total number of rows or columns.

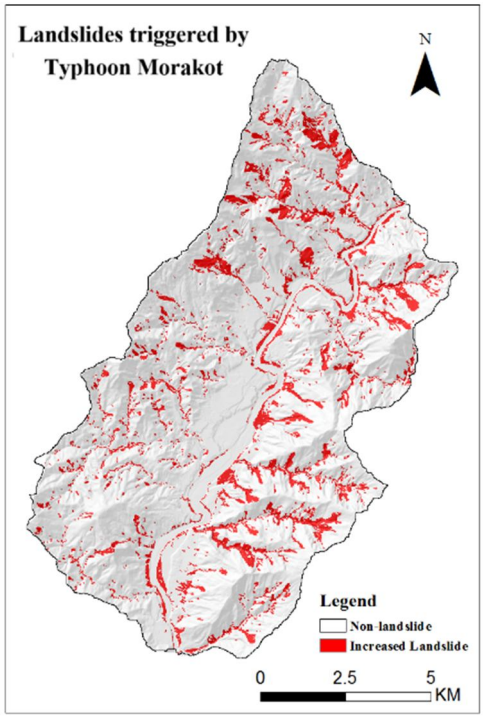

Figure 5 Landslide inventory map

Table 1 OBIA Segmentation Parameters

Parameter	Setting	Description
Segmentation Method	Multiresolution	Bottom-up region growing
Scale Parameter	30 (object size control)	Controls merging threshold
Shape	0.1	Controls spectral vs. shape weighting
Compactness	0.5	Controls object compactness
Typical Object Size	3–5 clusters per landslide	Captures internal variability

Table 2 GLCM Texture Extraction Parameters

Parameter	Setting	Description
Quantization Level	5 bits (32 levels)	Original images compressed to reduce sparse matrices
Window Size	3 × 3 pixels	Preserves local texture characteristics
Pixel Distance	1 pixel	Based on 3 × 3 window
Directions	0°, 45°, 90°, 135°	All four orientations averaged

3.3 Training Sample Selection

Sampling was designed to ensure that training data capture the characteristic signatures of event-induced landslides and stable terrain, with the Normalized Difference Sigma-naught Index (NDSI) serving as the primary criterion. NDSI quantifies the relative difference in backscatter between pre- and post-event SAR images and is particularly sensitive to abrupt changes in surface scattering associated with slope landslides. Landslide samples were therefore selected from areas exhibiting pronounced positive or negative NDSI values, indicating strong deviations in radar return consistent with ground disturbance. Conversely, non-landslide samples were extracted from zones where NDSI values remained close to zero, signifying stable surfaces with minimal backscatter change (Table 3).

$NDVI_{diff}$ was used as a secondary criterion to corroborate vegetation loss and surface exposure. Negative $NDVI_{diff}$ values, reflecting a transition from vegetated cover to bare soil, were required to coincide with the NDSI anomalies to classify landslide samples, while non-landslide samples were confirmed in areas showing negligible $NDVI_{diff}$ variation. This dual-index approach reduced the influence of noise, atmospheric effects, and geometric distortions inherent to SAR data, thereby improving the robustness of sample selection.

Using NDSI as the primary discriminant and $NDVI_{diff}$ as a complementary measure produces a balanced set of landslide and non-landslide samples that reflect both radar backscatter and spectral vegetation change. This sampling strategy ensures that the training data emphasize the most diagnostic characteristics of event-driven slope landslides and provide a strong foundation for subsequent classification and image-fusion analyses aimed at rapid emergency mapping.

3.4 Supervised Classification

An artificial neural network (ANN) framework (Figure 6) was employed to classify landslide and non-landslide objects derived from the OBIA and decision-level image fusion stages. Image segmentation combined with GLCM-derived textures generated object-level attributes from both optical ($NDVI_{diff}$) and SAR (NDSI) datasets, thereby capturing spectral changes, backscatter variation, and textural complexity within each landslide cluster. These heterogeneous features exhibit non-linear interactions that cannot be effectively modeled using traditional parametric classifiers, necessitating a more flexible approach.

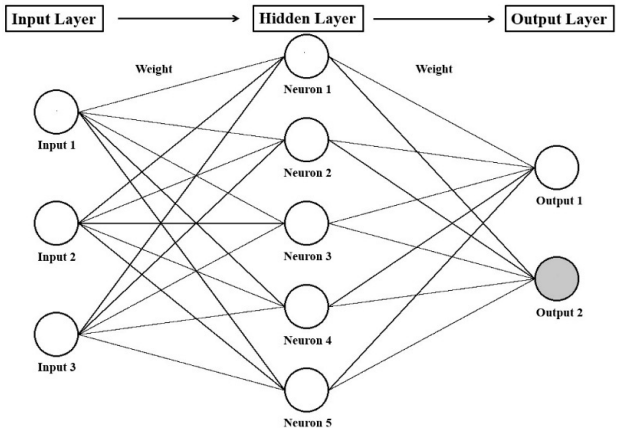

Figure 6 Schematic diagram of the Artificial Neural Network architecture

A back-propagation neural network (BPNN) implemented as a multilayer perceptron was selected due to its capacity to learn complex, non-linear decision boundaries from limited training samples (Table 4). During the forward pass, OBIA-derived features were propagated through the input and hidden layers to produce classification outputs. The backward pass computed the gradient of the loss function with respect to network weights, which were iteratively updated to minimize classification error between predicted and reference labels. This supervised learning process continued until convergence criteria were met, allowing the network to establish optimal internal representations for distinguishing landslide from non-landslide objects (Figure 7). By applying the BPNN to fused $NDVI_{diff}$ and NDSI features, the complementary strengths of optical and SAR data were integrated into a single probabilistic classification. This approach provided a robust and scalable means of producing rapid, event-driven landslide maps under conditions where optical imagery alone is insufficient due to cloud cover or adverse weather.

In the proposed framework, OBIA serves as an intermediate feature extraction and spatial aggregation stage that bridges raw image measurements and ANN-based classification. Specifically, multiresolution segmentation first partitions the fused $NDVI_{diff}$ and NDSI imagery into homogeneous objects representing candidate landslide units. For each object, statistical, spectral, and GLCM-based texture features are computed and summarized to form an object-level feature vector. These feature vectors, rather than pixel-level values, are subsequently used as input to the BPNN classifier. In this manner, OBIA transforms spatially correlated pixel information into meaningful analysis units, while the ANN learns nonlinear decision boundaries from the resulting object attributes. This object-to-network linkage enables efficient integration of spatial context, textural information, and multisource indices within a unified classification framework.

Table 3 Signatures of increased landslide and non-landslide areas in $NDVI_{diff}$ and NDSI images

Categories	$NDVI_{diff}$	NDSI
Increased Landslides		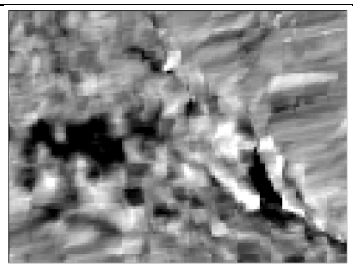
	Increased landslides are characterized by dark zones (negative values) in the $NDVI_{diff}$ image and pronounced signal variations (extreme values) in the NDSI image.	
Non-Landslide	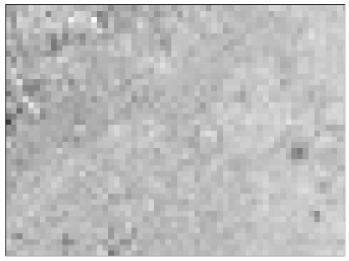	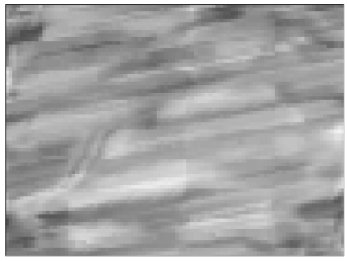
	In contrast to increased landslides, non-landslide areas exhibit minimal index variation, with values remaining close to zero in both $NDVI_{diff}$ and NDSI images.	

Table 4 ANN (BPNN) Classification Parameters

Parameter	Setting	Description
Network Type	Multilayer Perceptron	Supervised back-propagation network
Training Algorithm	Levenberg–Marquardt (LM)	Fast convergence for nonlinear optimization
Transfer Function	Sigmoid	Used in hidden and output layers
Hidden Layers	1	Single hidden layer
Hidden Neurons	6 / 12	Depends on input variables
Training Epochs	1000 / 2000	Based on model complexity
Output	Probability (0–1)	Object-wise landslide likelihood
Thresholding	Jenks Natural Breaks	Data-driven classification threshold

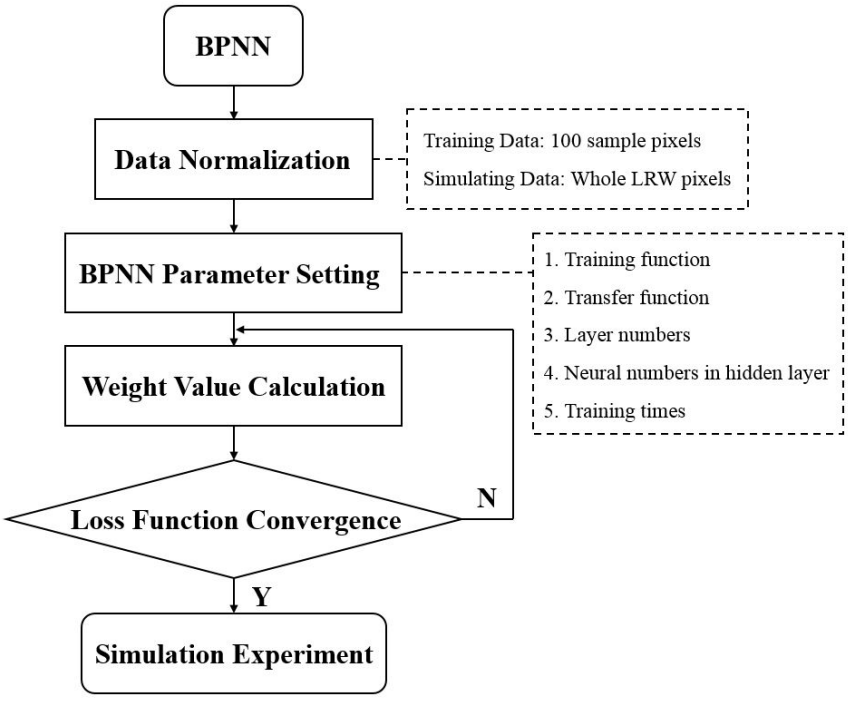

Figure 7 BPNN flow chart

The ANN produces object-wise probabilities ranging from 0 to 1, which require thresholding to classify landslide and non-landslide areas. To emulate emergency conditions without a reference inventory, the Jenks Natural Breaks (JNB) method (Jenks, 1967) was applied, as it iteratively minimizes within-class variance and maximizes between-class variance, yielding data-driven thresholds for robust landslide delineation.

4. Results and Discussion

Building on the object-based image analysis (OBIA) framework and the decision-level fusion strategy outlined above, four artificial neural network (ANN) classification models were developed to evaluate and simulate event-driven landslide mapping. (1) ANN-$NDVI_{diff}$ assesses the performance of cloud-free optical data for landslide detection, trained exclusively on six $NDVI_{diff}$-0912 texture images; (2) ANN-Cloud simulates emergency conditions where cloud-free optical imagery is unavailable, using six $NDVI_{diff}$-0815 texture images to test classification under adverse weather scenarios; (3) ANN-NDSI evaluates the capability of SAR data alone, trained on six NDSI texture images to capture backscatter-based changes; and (4) ANN-Fusion integrates six NDSI texture images with six $NDVI_{diff}$-0815 texture images to test decision-level fusion performance under conditions mimicking delayed acquisition of clear optical data.

Although stand-alone SAR imagery can effectively delineate large-scale landslides, the integration of optical and SAR observations was conducted to improve the robustness of emergency landslide mapping. Optical vegetation indices, such as $NDVI_{diff}$, are sensitive to vegetation loss and soil exposure, whereas SAR backscattering variations reflect changes in surface roughness and moisture conditions. These complementary characteristics enable more comprehensive characterization of landslide-induced surface disturbances. Moreover, SAR detection in mountainous terrain may be affected by geometric distortions, while optical imagery is often degraded by cloud cover. By integrating $NDVI_{diff}$ and NDSI within a decision-level fusion framework, the proposed approach enhances the spatial continuity and operational reliability of post-disaster landslide inventories.

4.1 Study Area and Typhoon Event

The Laonung River Watershed in Kaohsiung (Figure 8), southern Taiwan, covers about 117 km² and originates from the southwestern foothills of the Central Mountain Range. Steep, narrow valleys and highly fractured bedrock formed by folds, faults, and cleavage systems dominate the area (Mondini & Chang, 2014). Elevations range from 257 to 1673 m (mean 716 m), with 82% below 1000 m. Slopes vary from 0° to 71.2° (mean 26.9°, SD 12.6°), indicating rugged terrain. The Laonung River Watershed has a tropical monsoon climate with a mean annual temperature of 23 °C and ~3400 mm of highly seasonal rainfall (Chiang, 2017). Typhoon Morakot triggered extensive landslides and debris flows in this watershed.

Typhoon Morakot (2009) was the most destructive typhoon to hit southern Taiwan in recent decades. From 6–10 August it crossed the island from Hualien to Taoyuan, delivering a record 2749 mm of rainfall at Alishan—far exceeding the 1749 mm set by Typhoon Herb in 1996 (Lin & Jeng, 2000). The extreme precipitation caused widespread flooding, massive landslides, and debris flows. According to Tsai & Liu, 2015, Morakot isolated villages, left 693 dead and 97 missing, and inflicted about NT$16.5 billion in agricultural and infrastructure losses, highlighting its unprecedented destructive power.

4.2 ANN-$NDVI_{diff}$

The ANN-$NDVI_{diff}$ classification result (Figure 9) demonstrates the strong potential of optical imagery for mapping landslides triggered by Typhoon Morakot. Differences in spectral characteristics between disturbed and undisturbed terrain, combined with the temporal variation of NDVI, provide a powerful basis for detecting event-induced landslides. By calculating the NDVI difference between pre- (9 May 2009) and post-event (12 Sept. 2009) FORMOSAT-2 images, areas of vegetation loss are clearly distinguished from stable surfaces, enabling effective delineation of newly exposed soil and small or fragmented landslides, particularly in the southwestern area of the study area.

Despite these strengths, classification accuracy is constrained by atmospheric and illumination effects inherent to optical data. Cloud cover and terrain shadows in the 12 Sept. 2009 image produced NDVI values similar to bare soil, leading to false positives (Figure 10). For example, cloud-obscured areas C1 and C2 contained roughly 25 ha and 10 ha of redundant classified landslides (Figure 11–12), while shadowed forested slopes S1 and S2 were misclassified because topographic shading lowered NDVI values (Figure 13–14). These errors illustrate how weather conditions, solar angle, and terrain morphology can mask vegetation reflectance and confound spectral indices.

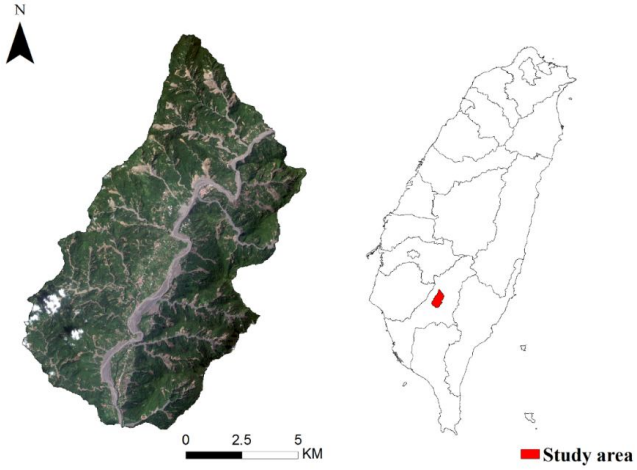

Figure 8 Study area: Laonung River Watershed overview (FORMOSAT-2, 12 Sept. 2009)

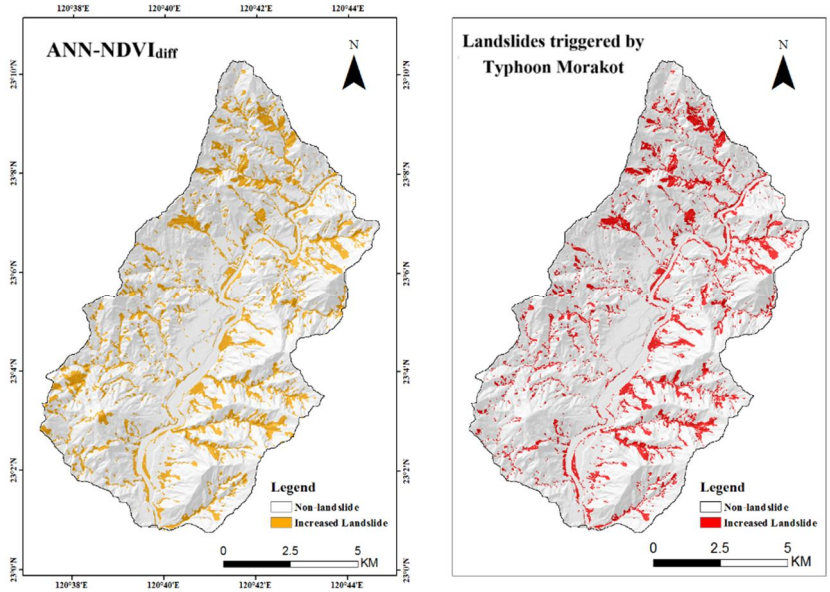

Figure 9 Comparison of the ANN-NDVI$_{diff}$ classification result with the ground truth

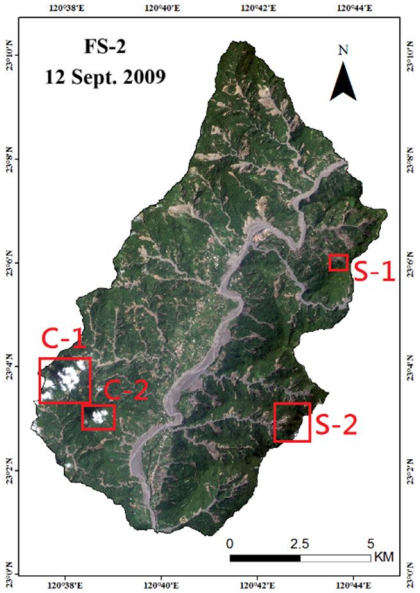

Figure 10 Locations of misclassification in the ANN-NDVI$_{diff}$ results: C-1 and C-2 correspond to areas affected by cloud cover, while S-1 and S-2 correspond to areas affected by terrain shadow

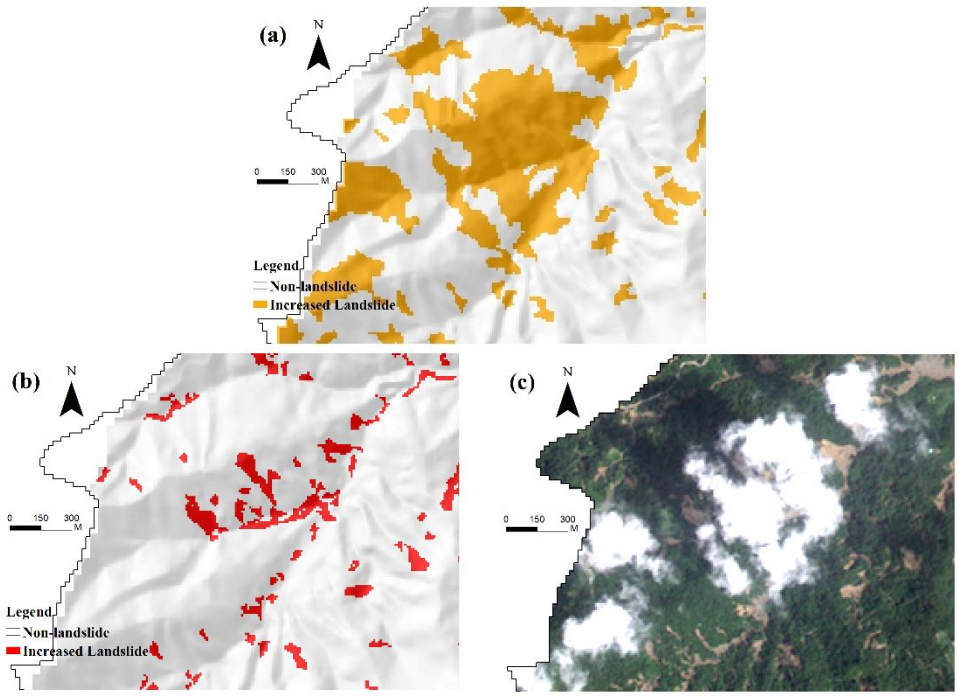

Figure 11 C-1 area. (a) ANN-NDVI$_{diff}$ classification result, where clouds are misclassified as landslides; (b) corresponding landslide inventory map; (c) FORMOSAT-2 image acquired on 12 Sept. 2009

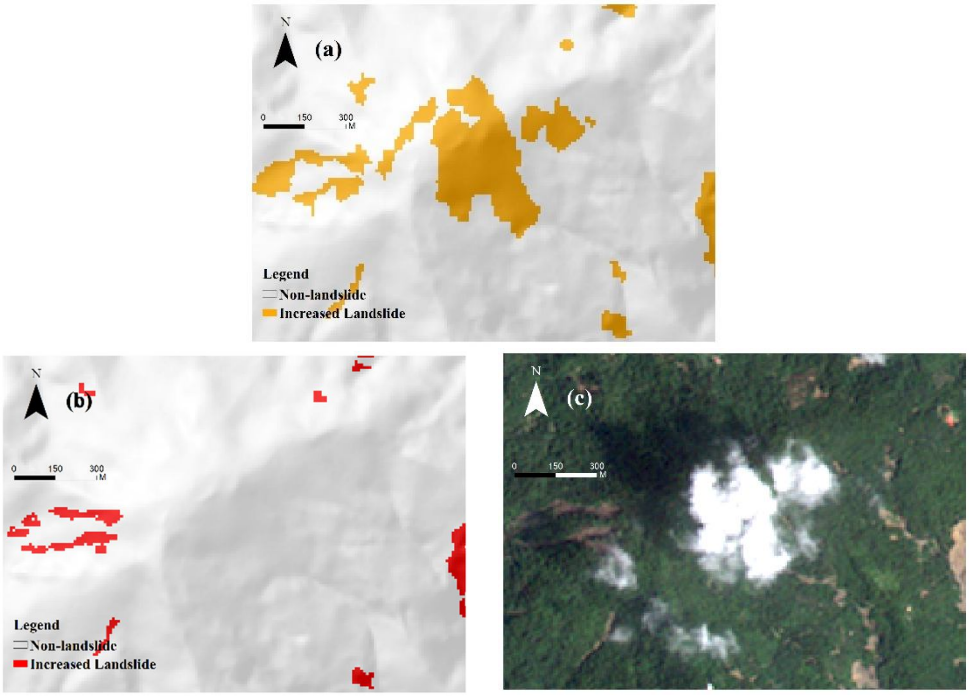

Figure 12 C-2 area. (a) ANN-NDVI$_{diff}$ classification result, where clouds and shadowed areas are misclassified as landslides; (b) corresponding landslide inventory map; (c) FORMOSAT-2 image acquired on 12 Sept. 2009

Overall, the object-based ANN-NDVI$_{diff}$ approach performs well in identifying landslides from high-resolution optical data, successfully capturing both large and small failures through combined spectral and temporal analysis of NDVI. However, its performance depends on timely cloud-free acquisitions. Because most Typhoon Morakot landslides occurred on 8 Aug. 2009 but the post-event image was not acquired until 12 Sept. 2009 due to persistent cloud cover, some temporal mismatches may have affected classification. While ANN-NDVI$_{diff}$ can produce accurate landslide maps under favorable conditions, these limitations underscore the reduced suitability of optical-only methods for rapid emergency mapping when immediate post-disaster imagery is unavailable.

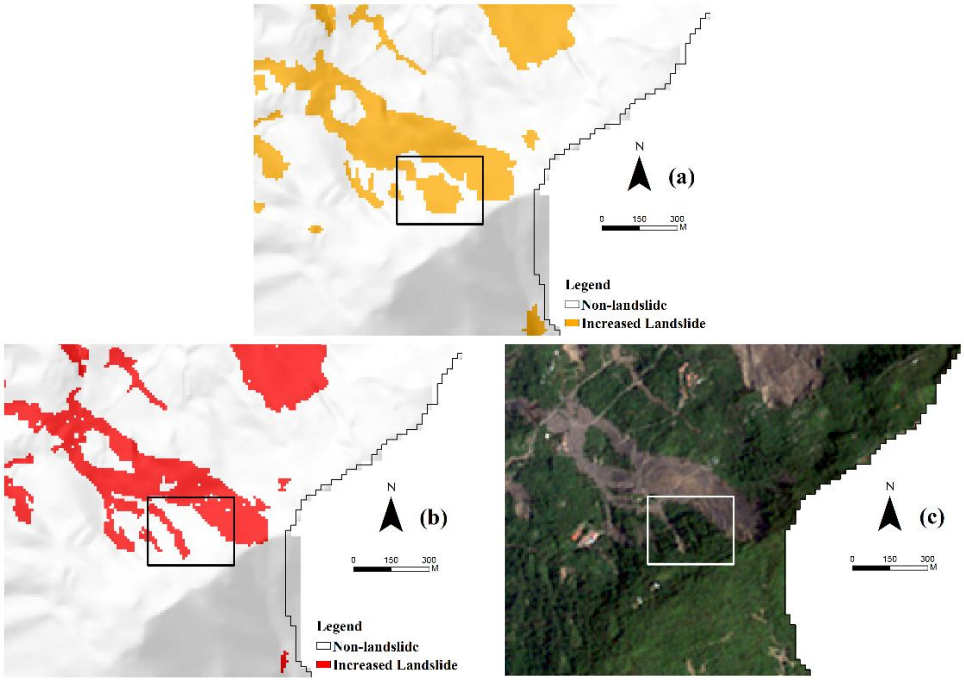

Figure 13 S-1 area. (a) ANN-NDVI$_{diff}$ classification result, where shadowed areas are misclassified as landslides; (b) corresponding landslide inventory map; (c) FORMOSAT-2 image acquired on 12 Sept. 2009

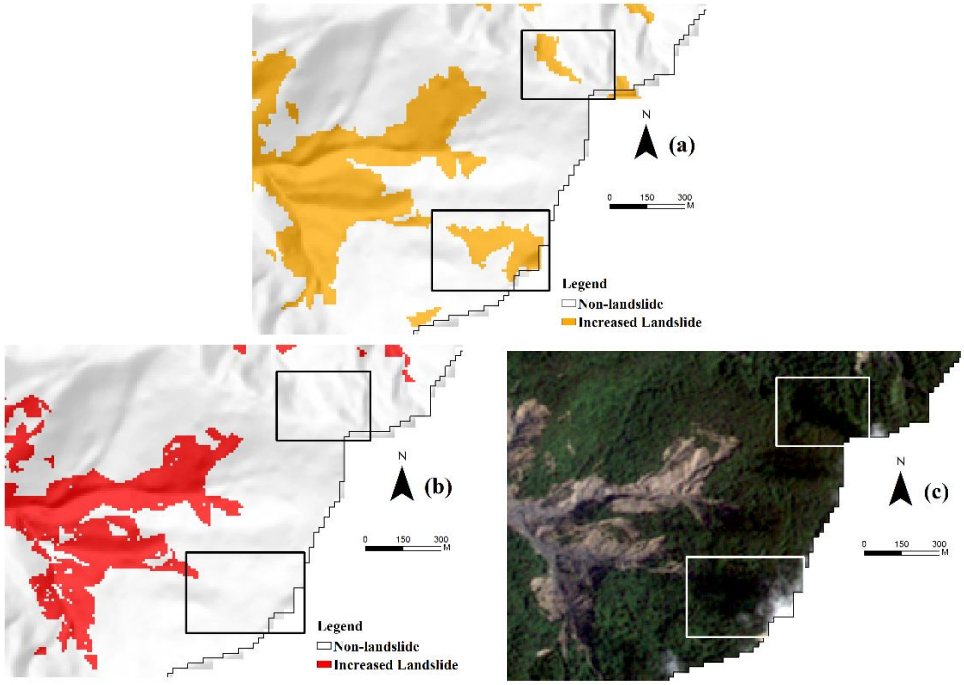

Figure 14 S-2 area. (a) ANN-NDVI$_{diff}$ classification result, where shadowed areas and clouds are misclassified as landslides; (b) corresponding landslide inventory map; (c) FORMOSAT-2 image acquired on 12 Sept. 2009

4.3 ANN-Cloud

The ANN-Cloud model was designed to replicate emergency mapping scenarios in which post-event optical images are severely obstructed by cloud cover. NDVI$_{diff}$ derived from the 15 Aug. 2009 scene was used, with cloud-covered areas masked and assigned a value of “0” to emulate the limited information available during adverse weather. As shown in Figure 15, this constraint markedly reduced classification performance relative to the inventory of Typhoon Morakot-triggered landslides. While the model successfully identified broad non-landslide areas, it substantially underestimated landslide extent, classifying most of the study area as non-landslide and omitting numerous true landslides. This outcome

reflects the heavy dependence of classification on $NDVI_{diff}$-0815 variables—particularly the mean value—under masked conditions. When large portions of an image are neutralized to zero values, the ANN is forced to rely on insufficient spectral cues, diminishing its ability to discriminate disturbed from undisturbed terrain. Although the resulting accuracy is weak, it underscores a critical limitation of optical imagery for emergency mapping, where the unavailability of clear post-event images inevitably compromises rapid analysis.

4.4 ANN-NDSI

The ANN-NDSI results (Figure 16) show that SAR-derived NDSI can serve as a stand-alone tool for rapid landslide mapping under emergency conditions. Exploiting L-band backscatter sensitivity to surface roughness, moisture, and slope orientation, NDSI effectively distinguishes disturbed from stable ground—even when clouds or low illumination prevent optical observation—allowing the model to delineate the extent and location of large landslides without post-event optical input.

Nevertheless, the results also highlight radar's inherent constraints. Foreshortening, layover, and shadowing in steep terrain distort or displace signals from small or fragmented landslides, which are often merged with adjacent stable areas during segmentation. These effects are strongest in the south-western area (Figure 17), where slopes face away from the ascending radar beam and failures are small and discontinuous, leading to underestimation. In contrast, the model performed better in the north-west (Figure 18), north-east (Figure 19), and south-east (Figure 20) areas, where larger, more coherent landslides—such as the ~50 ha event in the north-west—produced strong, contiguous backscatter signatures that the ANN classified and outlined more accurately.

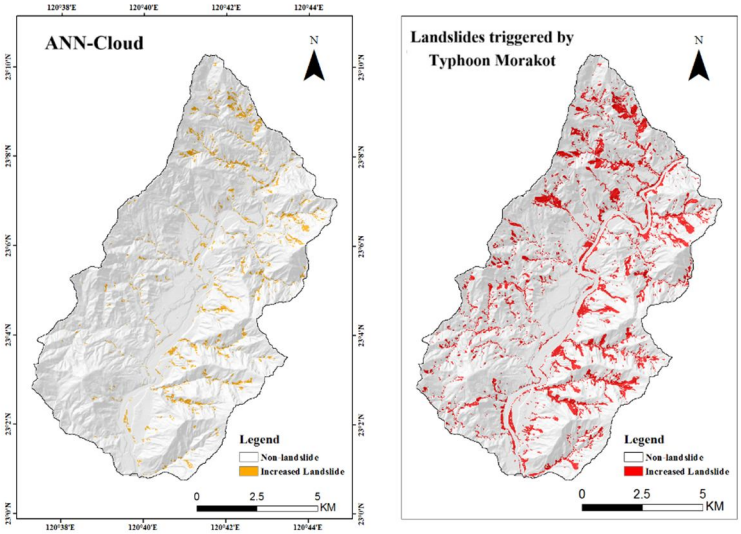

Figure 15 Comparison of the ANN-Cloud classification result with the ground truth

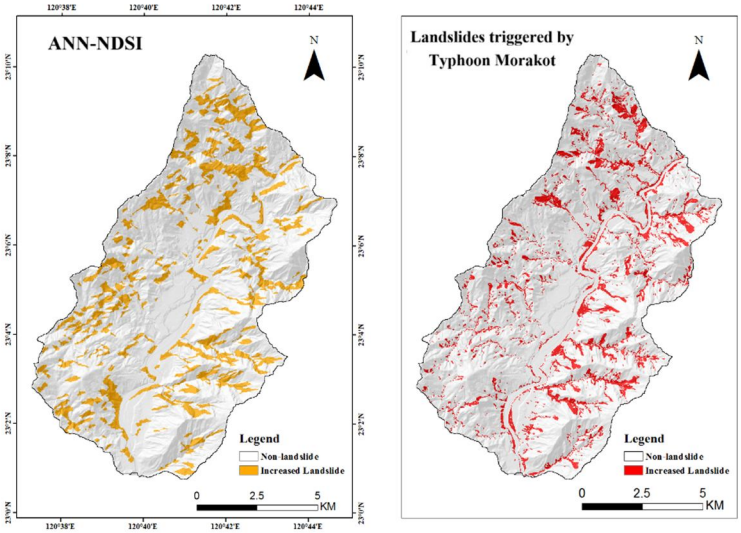

Figure 16 Comparison of the ANN-NDSI classification result with the ground truth

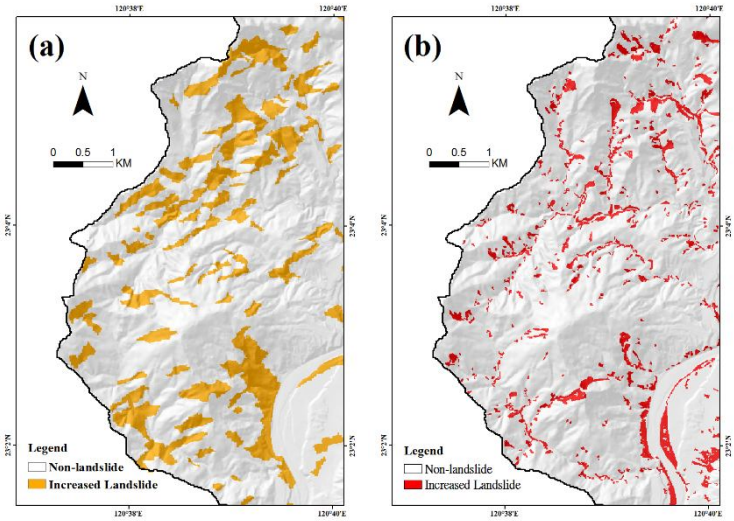

Figure 17 Southwestern area of the Laonong River Watershed: (a) ANN-NDSI classification result; (b) corresponding landslide inventory map

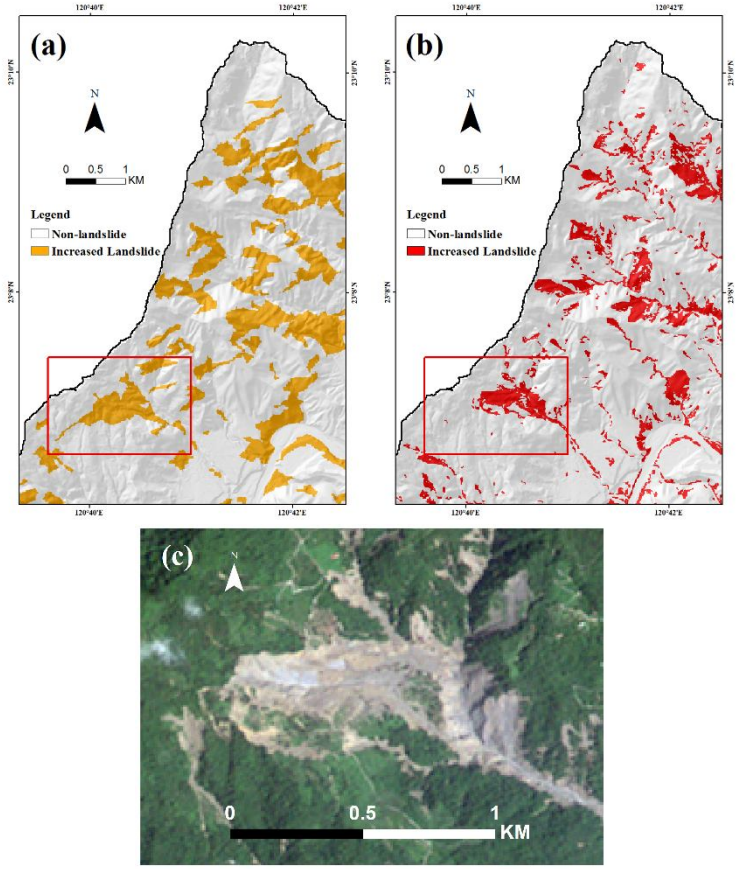

Figure 18 Northwestern area of the Laonong River Watershed: (a) ANN-NDSI classification result; (b) corresponding landslide inventory map; (c) FORMOSAT-2 image acquired on 12 Sept. 2009 showing the example landslide highlighted in the red box

Although the resulting footprints cannot perfectly coincide with ground-truth boundaries because of the inherent physical constraints of radar imaging, the overall performance confirms that NDSI provides a viable substitute for optical indices in emergency contexts. Under such conditions, SAR imagery enables rapid delineation of the approximate location and general extent of landslides owing to its all-weather and day–night acquisition capability. Nevertheless, its side-looking imaging geometry inevitably introduces distortions, including foreshortening, layover, and shadowing in mountainous terrain, which hinder precise spatial correspondence with reference inventories and constrain the applicability of

conventional statistical evaluation methods. As a result, rigorous quantitative accuracy assessment based on traditional metrics remains challenging for SAR-dominated results in complex topographic environments. Consequently, this study did not rely solely on conventional statistical indicators to validate fusion performance. Instead, the effectiveness of the proposed framework was primarily examined through comparative analysis of landslide location, areal extent, and overall spatial distribution patterns across optical-only, SAR-only, and integrated results. These analyses demonstrate that data fusion enhances mapping reliability by combining the rapid, weather-independent detection capability of SAR imagery with the high spatial fidelity and boundary definition provided by optical observations under favorable conditions.

4.5 ANN-Fusion

The ANN-Fusion model integrates $NDVI_{diff}$-0815 and NDSI texture features to simulate rapid post-event landslide mapping under conditions where cloud-free optical data are unavailable. As shown in the comparison between the fused classification output and the ground-truth inventory (Figure 21), the combined approach markedly improves emergency mapping performance relative to single-sensor models. By blending the spectral sensitivity of $NDVI_{diff}$ with the backscatter sensitivity of NDSI, the model captures both vegetation loss and radar-derived surface changes, allowing more complete delineation of disturbed slopes immediately after the typhoon. Although the fusion is dominated by the $NDVI_{diff}$ component—reflecting the stronger spectral contrast in optical data—the NDSI contribution becomes especially evident in the western

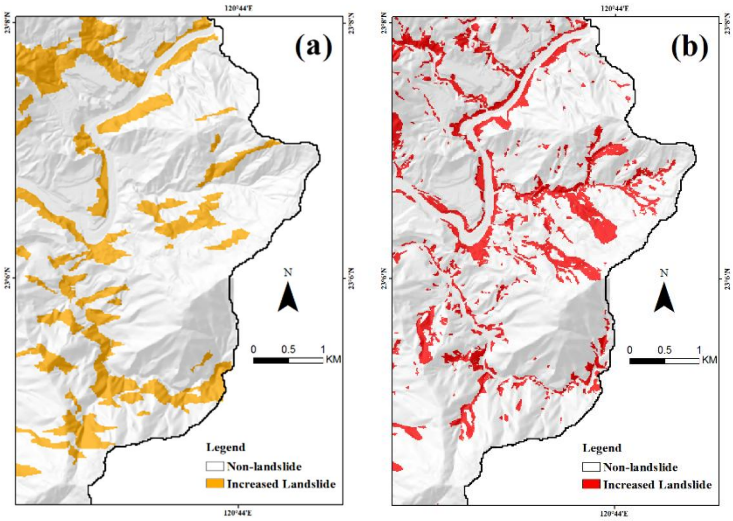

Figure 19 Southeastern area of the Laonong River Watershed: (a) ANN-NDSI classification result; (b) corresponding landslide inventory map

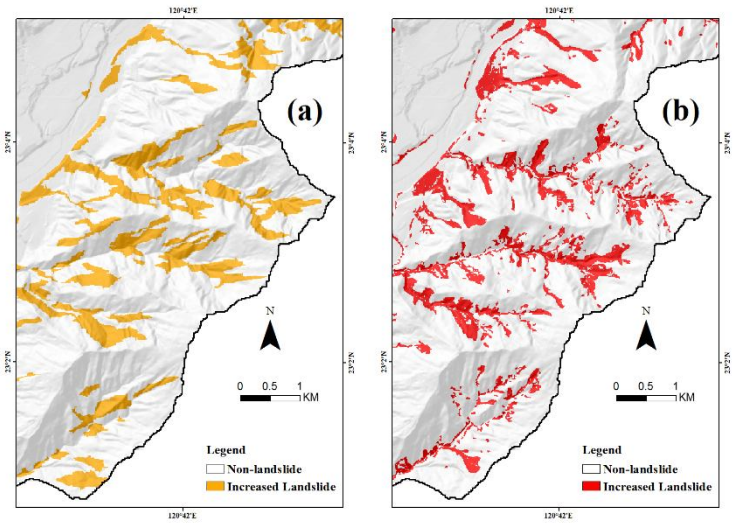

Figure 20 Southeastern area of the Laonong River Watershed: (a) ANN-NDSI classification result; (b) corresponding landslide inventory map

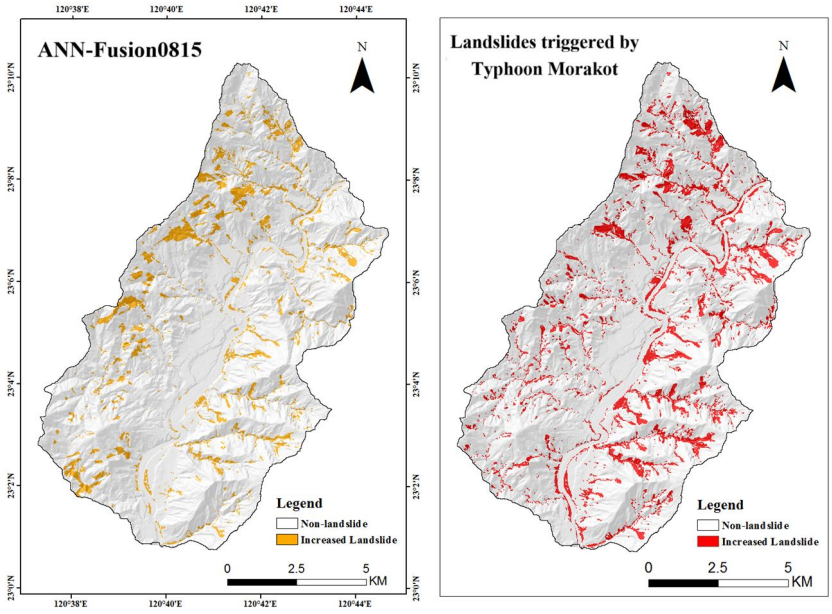

Figure 21 Comparison of the ANN-Fusion0815 classification result with the ground truth

portion of the study area where cloud cover masks large areas of the optical image. In these areas, radar backscatter differences supplement the missing optical signal and help recover landslide outlines that would otherwise be obscured. This complementary effect between optical and radar inputs enhances the robustness of the classification, yielding a more spatially coherent and realistic representation of landslide extent than either index alone. Consequently, ANN-Fusion0815 demonstrates the potential of decision-level image fusion to balance the strengths of optical and SAR data, providing a practical framework for rapid and reliable landslide inventory generation in emergency scenarios when clear optical imagery cannot be obtained.

5. Conclusions and Recommendation

This study presents an ANN-based decision-level image fusion framework within an OBIA environment for rapid landslide mapping after Typhoon Morakot. By combining $NDVI_{diff}$ from optical imagery with NDSI from L-band SAR backscatter, the approach exploits complementary spectral and radar information while avoiding typical co-registration challenges in rugged terrain. OBIA segmentation and texture extraction generate object-level features that improve classification robustness and reduce noise sensitivity.

Results show that $NDVI_{diff}$ performs well under clear conditions, NDSI provides a viable substitute when optical data are cloud-obstructed, and their fusion yields the most complete and coherent delineation of landslides under emergency conditions. Although SAR distortions and temporal gaps in optical imagery limit perfect agreement with ground truth, the fused ANN model effectively captures the extent and location of major landslides even under heavy cloud cover. This framework delivers timely, high-resolution landslide inventories to support disaster response, post-event assessment, and risk-reduction planning in other mountainous, cloud-prone regions.

Future research should refine the ANN–OBIA fusion framework to further enhance its operational value, integrate near-real-time SAR and optical data from multiple satellite constellations to reduce latency, develop algorithms to mitigate SAR distortions and improve small-landslide delineation, and embed the workflow into official disaster-response systems for broader application to other rapid-onset hazards.

References

Amarsaikhan, D., and Douglas, T., 2004. Data fusion and multisource image classification, International Journal of Remote Sensing, 25(17): 3529-3539, DOI: 10.1080/0143116031000115111.

Chen, H., He, Y., Zhang, L., Yang, W., Liu, Y., Gao, B., Zhang, Q., and Lu, J., 2023. A multi-input channel U-Net landslide detection method fusing SAR multisource remote sensing data, IEEE Journal of Selected Topics in Applied Earth Observations and Remote Sensing, 17: 1215-1232, DOI: 10.1109/JSTARS.2023.3339294.

Chen, Y.K., 2019. An artificial neural network approach for event landslide detection based on the integration of optical and SAR textures, Master Thesis, National Central University, Taiwan, ROC.

Chiang, S.H., 2017. The application of Sentinel-1 Synthetic Aperture Radar (SAR) imagery to the assessment of landslide reactivation, Soil and Water Conservation Bureau, Taiwan, ROC.

Colesanti, C., and Wasowski, J., 2006. Investigating landslides with space-borne Synthetic Aperture Radar (SAR) interferometry, Engineering Geology, 88(3-4): 173-199, DOI: 10.1016/j.enggeo.2006.09.013.

Coluzzi, R., Perrone, A., Samela, C., Imbrenda, V., Manfreda, S., Pace, L., and Lanfredi, M., 2025. Rapid landslide detection from free optical satellite imagery using a robust change detection technique, Scientific Reports, 15(1): 4697, DOI: 10.1038/s41598-025-89542-8.

Dai, F.C., and Lee, C.F., 2002. Landslide characteristics and slope instability modeling using GIS, Lantau Island, Hong Kong, Geomorphology, 42(3-4): 213-228, DOI: 10.1016/S0169-555X(01)00087-3.

Ez-zahouani, B., Teodoro, A., Kharki, O.E., Jianhua, L., Kotaridis, I., Yuan, X., and Ma, L., 2023. Remote sensing imagery segmentation in object-based analysis: A review of methods, optimization, and quality evaluation over the past 20 years, Remote Sensing Applications: Society and Environment, 32: 101031, DOI: 10.1016/j.rsase.2023.101031.

Fu, S., de Jong, S.M., Hou, X., de Vries, J., Deijns, A., and de Haas, T., 2024. A landslide dating framework using a combination of Sentinel-1 SAR and-2 optical imagery, Engineering Geology, 329: 107388, DOI: 10.1016/j.enggeo.2023.107388.

Furuta, R., and Tomiyama, N., 2008. A study of detection of Landslide disasters due to the Pakistan earthquake using ALOS data, in Proceedings of the 34th International Symposium on Remote Sensing of Environment, Sydney, Australia.

Guzzetti, F., Mondini, A.C., Cardinali, M., Fiorucci, F., Santangelo, M., and Chang, K.T. 2012. Landslide inventory maps: New tools for an old problem, Earth-Science Reviews, 112(1-2): 42-66, DOI: 10.1016/j.earscirev.2012.02.001.

Haeberlin, Y., Turberg, P., Retière, A., Senegas, O., and Parriaux, A., 2004. Validation of Spot-5 satellite imagery for geological hazard identification and risk assessment for landslides, mud and debris flows in Matagalpa, Nicaragua, The International Archives of the Photogrammetry, Remote Sensing and Spatial Information Sciences, XXXV-B3:273-278.

Haralick, R.M., Shanmugam, K., and Dinstein, I., 1973. Textural features for image classification, IEEE Transactions on Systems, Man, and Cybernetics, SMC3(6): 610-621, DOI: 10.1109/TSMC.1973.4309314.

Jenks, G.F., 1967. The data model concept in statistical mapping, International Yearbook of Cartography, 7: 186-190.

Jiang, P., Ma, Z., and Mei, G., 2025. Deep learning for potential landslide identification: Data, models, applications, challenges, and opportunities, EGUsphere, DOI: 10.5194/egusphere-2025-2158.

Jin, Y., Li, X., Zhu, S., Tong, B., Chen, F., Cui, R., and Huang, J., 2022. Accurate landslide identification by multisource data fusion analysis with improved feature extraction backbone network, Geomatics, Natural Hazards and Risk, 13(1): 2313-2332, DOI: 10.1080/19475705.2022.2116357.

Li, Y., and Xiao, X., 2025. Deep learning-based fusion of optical, radar, and LiDAR data for advancing land monitoring, Sensors, 25(16): 4991, DOI: 10.3390/s25164991.

Lin, M.L., and Jeng, F.S., 2000. Characteristics of hazards induced by extremely heavy rainfall in Central Taiwan—Typhoon Herb, Engineering Geology, 58(2): 191-207, DOI: 10.1016/S0013-7952(00)00058-2.

Liu, B., Wang, W., Wu, Y., and Gao, X., 2024. Attention swin transformer UNet for landslide segmentation in remotely sensed images, Remote Sensing, 16(23): 4464, DOI: 10.3390/rs16234464.

Mondini, A.C., and Chang, K.T., 2014. Combining spectral and geoenvironmental information for probabilistic event landslide mapping, Geomorphology, 213: 183-189, DOI: 10.1016/j.geomorph.2014.01.007.

Nichol, J.E., Shaker, A., and Wong, M.S., 2006. Application of high-resolution stereo satellite images to detailed landslide hazard assessment, Geomorphology, 76(1-2): 68-75, DOI: 10.1016/j.geomorph.2005.10.001.

Pohl, C., and Van Genderen, J.L., 1998. Review article multisensor image fusion in remote sensing: Concepts, methods and applications, International Journal of Remote Sensing, 19(5): 823-854, DOI: 10.1080/014311698215748.

Prakash, N., Manconi, A., and Loew, S., 2020. Mapping landslides on EO data: Performance of deep learning models vs. traditional machine learning models, Remote Sensing, 12(3): 346, DOI: 10.3390/rs12030346.

Selby, M.J., 1993. Hillslope Materials and Processes, Oxford: Oxford university press, p. 451.

Tetteh, G.O., Schwieder, M., Erasmi, S., Conrad, C., and Gocht, A., 2023. Comparison of an optimised

multiresolution segmentation approach with deep neural networks for delineating agricultural fields from sentinel-2 images, PFG–Journal of Photogrammetry, Remote Sensing and Geoinformation Science, 91(4): 295-312, DOI: 10.1007/s41064-023-00247-x.

Tsai, P.H., and Liu, C.W., 2015. Local economy growing at a steady pace: The case of the peasant farming project by the Taiwan Rural Front 1, In: Social Economy in China and the World, Pun, N., Ku, B.H., Yan, H., and Koo, A. (eds.), Routledge, London, pp. 248-259, DOI: 10.4324/9781315718286.

Tuo, W., Zeng, J., Wu, F., Wu, W., Wang, X., and Zhao, X., 2025. Landslide detection using multimodal data fusion and an improved Deeplabv3+ model, Scientific Reports, 16(1): 1383, DOI: 10.1038/s41598-025-31208-6.

Wang, H., Liu, X., Feng, G., Liu, P., Li, W., Liu, S., and Liao, W., 2025. Applicability of multi-sensor and multi-geometry SAR data for landslide detection in southwestern China: A case study of Qijiang, Chongqing, Sensors, 25(14): 4324, DOI: 10.3390/s25144324.

Weier, J., and Herring, D., 2000. Measuring Vegetation (NDVI & EVI), NASA Earth Observatory, Washington, DC, USA.

Zhang, Q., and Wang, T., 2024. Deep learning for exploring landslides with remote sensing and geo-environmental data: Frameworks, progress, challenges, and opportunities, Remote Sensing, 16(8): 1344, DOI: 10.3390/rs16081344.

應用類神經網路整合光學-SAR 紋理分析於緊急崩塌測繪

陳以耕[1*] 姜壽浩[2]

摘要

光學遙測影像可提供崩塌目錄製作所需之關鍵光譜資訊，但易受雲霧與天候影響而限制其應用。相較之下，合成孔徑雷達具全天候觀測能力且對地表後向散射變化敏感，可作為崩塌擾動之重要補充。本研究整合光學與雷達資料，發展快速且穩定之崩塌地辨識方法。方法採物件導向影像分析進行地物分割，並由多期影像推導標準化植被指數差值與標準化後向散射指數，計算六項灰階共生矩陣紋理特徵以表徵地物變化。本研究比較光學、雷達、受雲影響光學及光學－雷達融合四種情境。結果顯示，融合模式可提升崩塌地判釋之空間一致性與完整性；於高雲覆條件下，雷達亦能有效辨識大型崩塌地。顯示所提方法具良好作業效能，可應用於事件導向之快速製圖與災害評估。

關鍵詞：崩塌測繪、合成孔徑雷達、影像紋理、影像融合、人工類神經網路

[1] 國立臺灣大學土木工程學系 博士生
[2] 國立中央大學太空及遙測研究中心 副教授
[*] 通訊作者, E-mail: d10521008@ntu.edu.tw

收到日期：民國 114 年 10 月 15 日
修改日期：民國 115 年 01 月 07 日
接受日期：民國 115 年 02 月 04 日